Planetary and Space Science 116 (2015) 57–63

Contents lists available at ScienceDirect

Planetary and Space Science

journal homepage: www.elsevier.com/locate/pss

An AKARI infrared study of dust emission in Galactic bubbles indicative of large-scale cloud–cloud collisions

Y. Hattori *, H. Kaneda, D. Ishihara, M. Yamagishi, T. Kondo, H. Sano

Graduate School of Science, Nagoya University, Furo-cho, Chikusa-ku, Nagoya 464-8602, Japan

ARTICLE INFO

Article history:
Received 16 October 2014
Received in revised form
3 April 2015
Accepted 12 April 2015
Available online 23 April 2015

Keywords:
Infrared
Interstellar dust
Galactic bubbles
Massive stars

ABSTRACT

We report our systematic study on dust emission in massive star-forming regions indicative of large-scale cloud–cloud collisions, using the AKARI infrared (IR) all-sky survey data at wavelengths of 9, 18, 65, 90, 140, and 160 μm. We focus on the Galactic bubbles catalogued by Spitzer, which are categorized into two types of morphology, closed and broken bubbles. A broken bubble has a possibility of being created by a cloud–cloud collision, judging from its morphological similarity to the structure theoretically predicted as a product of the collision. Therefore we search for systematic differences in IR properties between the two types. We performed aperture photometry for 111 Spitzer bubbles and created the spectral energy distribution (SED) of each bubble. We decomposed the SED into polycyclic aromatic hydrocarbon (PAH), warm and cold dust components by model fitting, and calculated their luminosities, L_{PAH}, L_{warm} and L_{cold} respectively, by integrating each SED component as a function of the wavelength. We then investigated the total IR luminosity ($L_{TIR} = L_{PAH} + L_{warm} + L_{cold}$), the ratio of L_{PAH} to L_{TIR} and the ratio of L_{warm} to L_{TIR} as a function of the bubble radius. As a result, we find systematic differences between the closed and broken bubbles for the former two relations. We discuss the implications of the differences for the scenario of the large-scale cloud–cloud collisions.

1. Introduction

Young massive stars are often embedded deep inside the dense molecular clouds. Since they are severely affecting the state of the ambient interstellar medium (ISM) through intense UV radiation, the activity of the massive star formation can be understood by investigating the properties of the ambient ISM. However, the formation process of a massive star itself is insufficiently understood; one serious problem is that the feedback of UV radiation pressure to accreting gas stops the growth of massive stars (Wolfire and Cassinelli, 1987). To solve this problem, an efficient gas accretion is needed. For examples, several processes of gas compression due to supernova explosion, radiation pressure from massive stars, or large-scale magnetic force have been discussed (e.g., Elmegreen and Lada, 1977; Ishihara et al., 2007). One of the most effective scenarios is a large-scale cloud–cloud collision, which is theoretically suggested in the previous work (Habe and Ohta, 1992; Inoue and Fukui, 2013). Habe and Ohta (1992) found that a collision between two molecular clouds induces strong bow shocks which disrupt parental molecular clouds and create gravitationally unstable cloud cores as a consequence of shock compression. Massive stars can be formed by the gravitational collapse of the unstable cloud cores. Recently, several pieces of observational evidence for this scenario have been found in Galactic massive star-forming regions by CO observations with the NANTEN/NANTEN2 radio telescopes (Furukawa et al., 2009; Torii et al., 2011; Fukui et al., 2014).

Infrared (IR) observations of massive star-forming regions provide information on thermally excited dust grains including polycyclic aromatic hydrocarbons (PAHs), which are distributed around massive stars. Since these components absorb a dominant fraction of UV photons from young massive stars and re-radiate the absorbed energy at mid- and far-IR wavelengths, we can measure the total energy of embedded sources from the total IR dust emission. Additionally, we can reveal complicated geometry of star-forming regions with the PAH emission which traces the surfaces of photo-dissociation regions (PDRs) as boundaries of heating sources and molecular clouds.

A systematic IR study of massive star-forming regions with Spitzer has provided the catalogue of the Galactic bubbles (Churchwell et al., 2006). These bubbles are called Spitzer bubbles, which have shell-like structures identified in the Spitzer/IRAC 8 μm band. In this catalogue, the bubbles are classified into two types of morphology: closed and broken bubbles. A closed bubble has a well-defined shell structure in the mid-IR band, which has been considered to be formed by ionizing radiation or strong

* Corresponding author. Tel.: +81 52 7893540.
E-mail address: hattori@u.phys.nagoya-u.ac.jp (Y. Hattori).

http://dx.doi.org/10.1016/j.pss.2015.04.006
0032-0633/

stellar wind of central massive stars. On the other hand, a broken bubble has an imperfect shell structure, which does not cover the whole direction. The latter type of bubbles possesses a morphological similarity to the structure theoretically predicted to be produced by a cloud–cloud collision (Habe and Ohta, 1992). For this reason, broken bubbles have a possibility of being created by cloud–cloud collisions.

In this paper, we search for difference in the properties of dust emission between closed bubbles and broken bubbles to investigate the possible contribution of cloud–cloud collisions to massive star formation. We create mid- to far-IR spectral energy distributions (SEDs) of the Spitzer bubbles to decompose the SEDs into PAH, warm and cold dust components. Then, based on the IR luminosity of each component, we investigate the relations of the total luminosity and luminosity ratios with the bubble radius.

2. Sample selection and data analysis

We defined the following criteria for our sample selection. First, we selected Spitzer bubbles, the distances of which were estimated in the previous works (Beaumont and Williams, 2009; Churchwell et al., 2006; Deharveng et al., 2010; Pavel and Clemens, 2012; Watson et al., 2010; Zhang et al., 2013). Second, we checked all the images of each bubble derived from the AKARI all-sky surveys at wavelengths of 9, 18, 65, 90, 140, and 160 μm to eliminate the bubbles contaminated by nearby objects. As a result, we obtain 111 bubbles as our sample, including 69 closed bubbles and 42 broken bubbles. Fig. 1 shows examples of the AKARI 9 μm images of our sample for five closed bubbles (N4, S44, S137, S14 and S143) and five broken bubbles (N5, S76, S186, S145 and N107).

We performed surface aperture photometry for the sample bubbles using the AKARI all-sky survey data in the six bands. We set the photometry aperture sizes twice as large as the bubble radii given in Churchwell et al. (2006) to cover the whole far-IR distribution. If other objects are included in the apertures, we adjust the sizes and the positions to exclude them. We subtract a sky level in the photometry. The sky level is determined by an annular region of a width ~10″ (9 and 18 μm) or ~30″ (65, 90, 140 and 160 μm), adjacent to the circular aperture. As flux uncertainties, we consider both random and systematic errors. The random error is estimated from the fluctuation of the sky brightness in each image. The systematic errors for the mid-IR (9 and 18 μm bands) and far-IR fluxes (65, 90, 140 and 160 μm bands) are given by Ishihara et al. in prep. and Doi et al. in prep., respectively. Then, using the photometric results, we created SEDs of the bubbles. By model fitting, we decomposed the SED into PAH, warm and cold dust components. In the fitting, we used the PAH model spectrum given in Draine and Li (2007) and modified blackbody spectra with the emissivity power-law index β of 2 for other two dust components, where free parameters were the amplitudes of the three components and the temperature of the warm dust component. The temperature of the cold dust was fixed at 18 K, because we could not constrain the cold dust temperature very well for every sample bubble. The temperature of 18 K was estimated by fitting the model to the SED averaged over the total sample; the SED of each bubble is normalized by its 160 μm flux and then added. Fig. 2a shows the SED thus averaged. The cold dust temperature derived from the fitting to the averaged SED is 18.4 ± 1.2 K. Therefore we adopt 18 K as a typical cold dust temperature, although the temperature is not strictly constrained by the far-IR data because of lack of data beyond 160 μm. Fig. 2b shows an example of the SED fitting results. The reduced χ^2 values thus derived indicate that the model is acceptable for most of the bubble SEDs. The best-fit temperature of the warm dust component ranges from 58 to 81 K for the closed and from 60 to 75 K for the broken bubbles. The resultant SEDs show an overall agreement with the IRAS and Spitzer flux densities within uncertainties. The IR luminosity of the PAH, warm and cold dust components, $L_{\rm PAH}$, $L_{\rm warm}$ and $L_{\rm cold}$ respectively, are estimated by integrating each component as a function of the wavelength for a range of 5–1000 μm. We derived the bubble radius, R, from the angular radius (Churchwell et al., 2006) and the distance of each bubble.

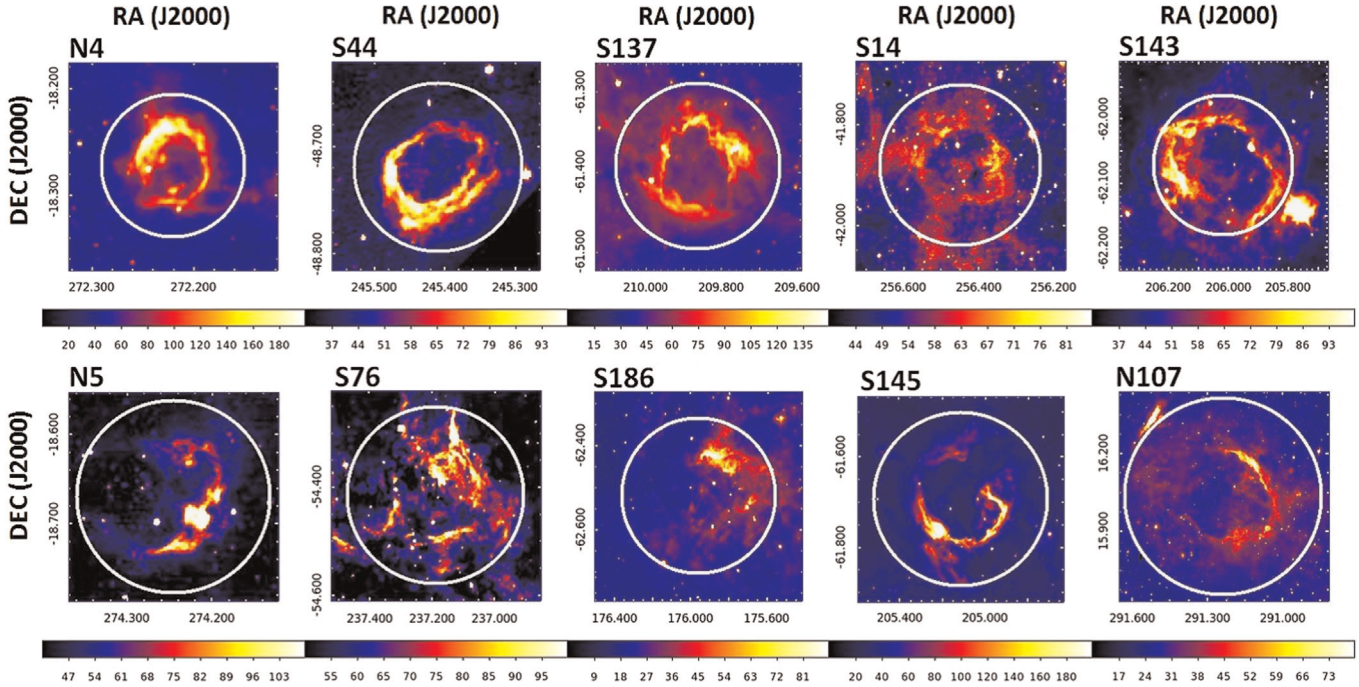

Fig. 1. Examples of the AKARI 9 μm images of our sample. The upper five panels correspond to closed bubbles, while the lower five panels correspond to broken bubbles. Circles indicate the aperture sizes used for surface photometry. The color levels are given in units of MJy sr^{-1}. (For interpretation of the references to color in this figure caption, the reader is referred to the web version of this paper.)